Energy 283 (2023) 129053

Contents lists available at ScienceDirect

Energy

journal homepage: www.elsevier.com/locate/energy

# Analytical temperature estimation process of the air supply system of the proton exchange membrane fuel cell stack in fuel cell electric vehicles

Dong-Min Kim [a], Jun-Woo Chin [b], Jae-Hyun Kim [c], Myung-Seop Lim [c,*]

[a] Department of Automotive Engineering, Honam University, Gwangju 62399, Republic of Korea
[b] Advanced Powertrain R&D Department, Korea Automotive Technology Institute, Cheonan 31214, Republic of Korea
[c] Department of Automotive Engineering, Hanyang University, Seoul 04763, Republic of Korea

ARTICLE INFO

*Keywords:*
Balance of plant
Centrifugal compressor
Gaussian process model
Lumped parameter thermal network
Thermal management
Ultra-high-speed motor

ABSTRACT

The air supply system of the proton exchange membrane fuel cell stack in fuel cell electric vehicles should be included as one of the components of the balance of plant. However, the air supply system consists of a centrifugal air compressor, driven by an ultra-high-speed motor. Therefore, there occurs a large amount of thermal energy from losses and the temperature of the air supply system should be considered. Accordingly, this study suggests the temperature estimation process for an air supply system based on a lumped parameter thermal network (LPTN). First, performance modeling is introduced using not only the empirical approach but also electromagnetic finite element analysis (FEA). Subsequently, thermal modeling based on the LPTN is presented. For this procedure, optimization techniques, screening, and surrogate model-based optimization are used. Finally, the results of LPTN construction are investigated. Furthermore, an additional experiment is conducted, and the result of this study is verified.

## 1. Introduction

Global attempts have been made to reduce greenhouse gas (GHG) emissions according to the Paris Agreement [1]. In addition, several commercial vehicle manufacturers have announced plans to discontinue the production of pure internal combustion engine (ICE) vehicles [2]. Owing to this trend, governments worldwide are attempting to promote electric vehicle (EV) adoption [3]. In addition, hydrogen-based vehicles have received attention, and attempts are being made to use hydrogen as a gas for combustion engines [4]. However, most hydrogen-based vehicles are fuel cell electric vehicles (FCEVs), and the market size of FCEVs is growing [5]. Similarly, the FCEV is treated as a candidate for future eco-friendly mobility [6,7]. The fact that FCEVs purify the air and emit only pure water presents several advantages. Furthermore, compared with battery electric vehicles (BEVs), FCEVs require less refueling time and have a greater driving range.

However, unlike the lithium-ion battery, the fuel cell (FC) needs auxiliary parts. The FC stack operation requires a water and thermal management system, fuel supply system, and air supply system. The water management system controls the flow of water from the hydrogen–oxygen reactions and humidity of the supplied oxygen to the FC stack. The thermal management system adequately performs system cooling. The fuel supply system manages the hydrogen supply, including the pressure control and recirculation of the exhausted hydrogen. In addition, the air supply system manages the oxygen supply, including the flow rate, pressure control, and dust filtering. These components are called the Balance of plant (BOP), and their configuration is shown in Fig. 1.

The air supply system affects the FC stack operation directly. Based on the air supply system performance, the power density, efficiency, and output voltage of the FC stack can differ [8–11]. The air supply system intakes outside air during vehicle driving and compresses the intake air using a centrifugal compressor. Typically, a centrifugal compressor is driven by an ultra-high-speed (UHS) motor. Therefore, large losses occur in the inverter, UHS motor, and bearings. This results in a temperature rise in the air supply system, and the performance of the UHS motor can be affected. Subsequently, UHS motor performance is directly linked to the air compression performance, and temperature estimation of the air supply system is essential. Therefore, we should consider the temperature of the air compressor in the thermal management of FCEV. In addition, a study on thermal management considering the temperature of air supply systems shows the importance of air supply systems' temperature [12].

Recently, numerous studies on the air compressor of air supply systems have been conducted. Wang et al. studied a double-scroll-type air compressor [13]. Wang et al. Geng et al. and He et al. investigated a twin-screw-type air compressor [14–16]. However, a large portion

* Corresponding author.
*E-mail address:* myungseop@hanyang.ac.kr (M.-S. Lim).

https://doi.org/10.1016/j.energy.2023.129053
Received 5 April 2023; Received in revised form 26 July 2023; Accepted 10 September 2023
Available online 16 September 2023

## Nomenclature

### Abbreviations

| | |
|---|---|
| 2D | Two Dimensional |
| 3D | Three Dimensional |
| ANOVA | Analysis of Variance |
| BEV | Battery Electric Vehicle |
| BOP | Balance of Plant |
| CFD | Computational Fluid Dynamics |
| DOE | Design of Experiment |
| EV | Electric Vehicle |
| FC | Fuel Cell |
| FCEV | Fuel Cell Electric Vehicle |
| FEA | Finite Element Analysis |
| GHG | Greenhouse Gas |
| GPM | Gaussian Process Modeling |
| ICE | Internal Combustion Engine |
| LPTN | Lumped Parameter Thermal Network |
| NRMSE | Normalized Root Mean Squared Error |
| OA | Orthogonal Array |
| RMSE | Root Mean Squared Error |
| SPMSM | Surface-mounted Permanent Magnet Synchronous Motor |
| UHS | Ultra-High-Speed |

### List of symbols

| | |
|---|---|
| $\eta_{em}$ | Efficiency of electric motor |
| $\eta_{inv}$ | Efficiency of inverter |
| $\omega$ | Electrical rotational angular speed |
| $\omega_m$ | Mechanical rotational angular speed |
| $\Psi_a$ | Armature linkage flux |
| $\rho$ | Density of lumped components |
| $\theta_{1,2}$ | Inner and outer temperatures in radial direction |
| $\theta_{3,4}$ | Front and rear temperatures in axial direction |
| $\theta_m$ | Representative temperature of lumped components |
| $C$ | Heat capacity of lumped components |
| $c$ | Specific heat of lumped components |
| $f$ | Objective function |
| $i_{d,q}$ | $d$–$q$ axis currents |
| $i_{od,oq}$ | $d$–$q$ axis currents subtracting iron loss component |
| $k_a$ | Thermal conductivity of axial direction |
| $k_r$ | Thermal conductivity of radial direction |
| $L$ | Axial length of lumped components |
| $L_{d,q}$ | $d$–$q$ axis inductances |
| $n_s$ | Number of sampling points |
| $p$ | Differential operator |
| $P_p$ | The number of pole pairs |
| $r_{1,2}$ | Inner and outer radii of lumped components |
| $R_{a,1,2}$ | Thermal resistances of axial direction |
| $R_{a,m}$ | Compensation thermal resistance of axial direction |
| $R_a$ | Armature winding resistance |
| $R_I$ | Equivalent resistance for iron loss |
| $R_{r,1,2}$ | Thermal resistances of radial direction |
| $R_{r,m}$ | Compensation thermal resistance of radial direction |
| $T$ | Torque |
| $T_c$ | Cumulative temperature |
| $t_c$ | End time of transient condition |
| $T_{EXP}$ | Experimentally measured temperature |
| $T_{LPTN}$ | Estimated temperature from LPTN |
| $T_s$ | Saturation temperature |
| $t_s$ | Temperature saturation time |
| $u$ | Generated heat of lumped components |
| $v_{d,q}$ | $d$–$q$ axis voltages |
| $v_{od,oq}$ | $d$–$q$ axis induced voltages |
| $W_C$ | Copper loss |
| $W_E$ | Rotor eddy current loss |
| $W_{inv}$ | Input power of inverter |
| $W_I$ | Iron loss |
| $W_{mot}$ | Input power of electric motor |

of the other studies has focused on centrifugal air compressors. Some studies have dealt with the aerodynamic performance optimization of the compression part through various approaches, such as computational fluid dynamics (CFD) and data mining strategies [17,18]. In addition, research on oil-free bearings for FCEV air compressors has been conducted [19]. Inevitably, considerable research on UHS motors has been conducted, not only for design but also for control [20–22].

However, the thermal aspects of FCEVs have not received considerable attention. Kim et al. conducted study on the thermal management of FCEV [23]. However, the temperature of the air supply system was omitted. Hu et al. suggested an enhancement of the cooling performance of the air supply system [24]. However, temperature monitoring could not be achieved. Im et al. studied the temperature estimation of a UHS motor reflecting the precisely calculated motor losses [25]. However, other losses, such as the bearing loss and inverter loss, and the overall compressor structure were not considered.

These days, studies on lumped parameter thermal network (LPTN) have been intensively conducted [26–40]. In Table 1, the features of the target of these studies are organized. Most of the study focused on LPTN modeling for single motors. Only Zhang et al. and Jeffrey et al. tried to model the LPTN of the integrated inverter and overall system [36,37]. On the other hand, the considered cooling method for the target motor varied, including air cooling, water cooling, and oil cooling. However, combined cooling methods such as air cooling with a water jacket were not considered. Additionally, the target motor's maximum power range was wide enough. However, the maximum speed range was not very broad; the highest operational speed was 16 krpm.

This study proposes a temperature estimation process considering the overall air supply system and UHS motor characteristics. The aerodynamic and electrical performances are both modeled, and thermal modeling is performed based on a LPTN. In addition, the maximum speed of the target motor was 100 krpm, which can arouse large amounts of losses and uncertainties of atmospheric conditions. Moreover, not only the water cooling channel in the housing but also the air cooling channel in the air hole of the shaft was considered. Furthermore, the proposed temperature estimation process is validated experimentally. The contributions of this study can be summarized as follows.

- Performance modeling methodology of the air supply system is introduced.
- Application of the lumped parameter thermal modeling concept to the overall compressor system is presented.
- Determination process of the uncertain coefficients of lumped parameter thermal network is suggested.

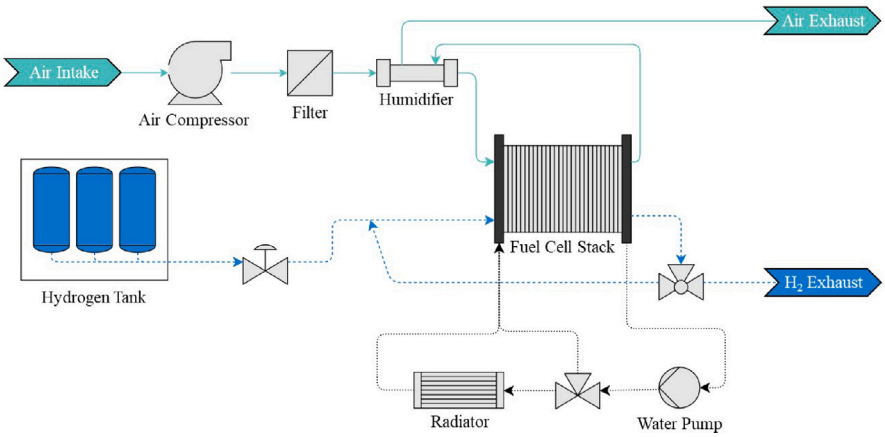


**Fig. 1.** Balance of plant for fuel cell stack.

**Table 1**
Target of recent studies on lumped parameter thermal network.

| Author (year) | Modeling target | Cooling method | Maximum speed (krpm) | Maximum power (kW) | Ref. |
|---|---|---|---|---|---|
| Li et al. (2023) | Motor only | Air cooling | 3.6 | 2.1 | [26] |
| Le et al. (2023) | Motor only | Water cooling | 4 | 60 | [27] |
| Cao et al. (2023) | Motor only | Water cooling | 6 | 100 | [28] |
| Gronwald et al. (2023) | Motor only | Oil cooling | 6 | 100 | [29] |
| Park et al. (2023) | Motor only | Oil cooling | 11 | 35 | [30] |
| Sun et al. (2023) | Motor only | Air cooling | 1 | 3.1 | [31] |
| Liu et al. (2023) | Motor only | Water cooling | 12 | 65 | [32] |
| Wöckinger et al. (2023) | Motor only | Air cooling | 7.1 | 0.1 | [33] |
| Chen et al. (2022) | Motor only | Water cooling | 0.5 | 2 | [34] |
| Wang et al. (2022) | Motor only | Oil cooling | 8 | 130 | [35] |
| Zhang et al. (2022) | Overall system | Water cooling | 16 | 160 | [36] |
| Jeffrey et al. (2022) | Motor, Inverter | Air cooling | 8 | 160 | [37] |
| Chattopadhyay et al. (2022) | Motor only | Water cooling | 7 | 11.5 | [38] |
| Sequeira et al. (2022) | Motor only | Water cooling | 10.4 | 80 | [39] |
| Zarghani et al. (2022) | Motor only | Air cooling | 0.9 | 2 | [40] |

- Temperature estimation result through the suggested process is experimentally verified.

The organization of this paper is as follows. First, the performance modelings for the aerodynamic and electrical aspects are introduced. Second, the application of the LPTN concept to air supply system thermal modeling is presented. Third, the uncertain coefficients of the LPTN for the air supply system are listed. Subsequently, the uncertain coefficients determination process based on optimization techniques is proposed. Finally, the LPTN construction result is confirmed, and the experimental verification through an additional test is explained.

## 2. Performance modeling

This section focuses on the performance modeling of the air supply system, which is the object of the thermal modeling in the next section. As shown in Fig. 2, the air supply system consists of a compression part, electric motor part, and controllers. Therefore, to predict the temperature of the air supply system, the losses of the electric motor should be derived according to the compression performance. Accordingly, the performance modeling in this section focused on the air compression performance and loss of the electric motor of the air compressor.

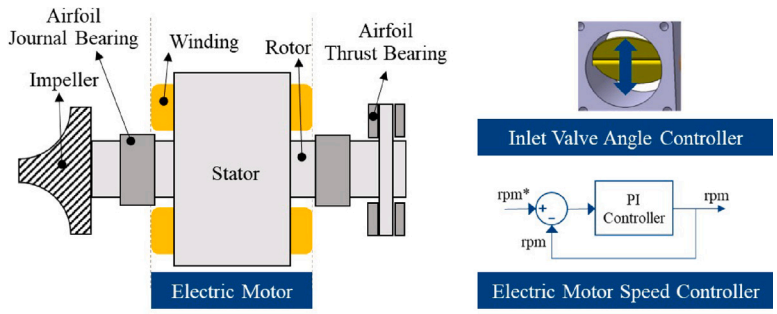


**Fig. 2.** Configuration of the air supply system.

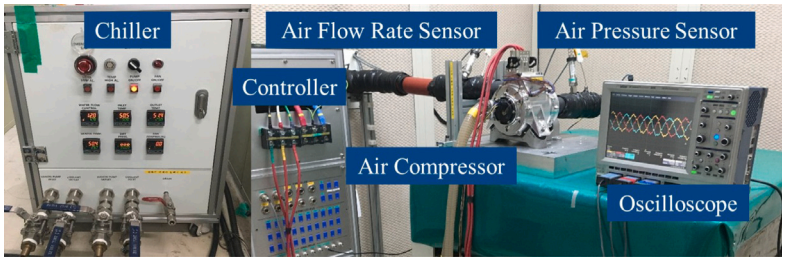


(a)

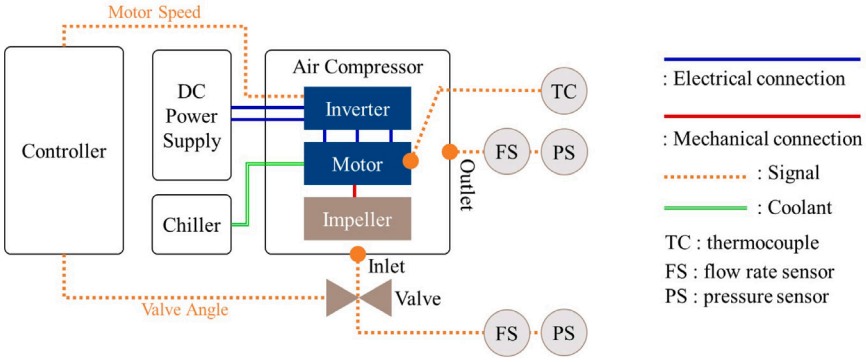


(b)

**Fig. 3.** Test bench setup (a) actual photo and (b) schematic diagram.

### 2.1. Compression part

The air compression performance was modeled based on the empirical methodology. For this modeling, an air supply experiment bench was built, as described in Fig. 3. The prototype air compressor was installed on the test bed, and the inlet and outlet of the air compressor were piped into the intake and exhaust air, respectively. In addition, air flow rate and air pressure sensors were installed at the inlet and outlet of the air compressor. Additionally, a water pump with a chiller was connected to the water-cooling channel of the air compressor with a hose. Furthermore, the input current of the electric motor was captured by an oscilloscope, and the input power of the controller was measured using a power analyzer equipped outside of this picture.

With this experiment setup, the air flow rate and outlet air pressure were measured according to the various inlet valve angles and electric motor speeds. Based on the measured points and polynomial fitting, the air flow rate and outlet pressure models were produced, as shown in Fig. 4. Table 2 presents polynomial fitting evidence. For fitting the order number of the equations, the value of the R-squared and root-mean-squared error (RMSE) was used as the goodness of fit.

**Table 2**
Modeling evidence of the compression performance using polynomial fitting.

| Fitting equation | Goodness of fit | Value | |
|---|---|---|---|
| | | Air flow rate | Outlet pressure |
| 2nd order | R-squared | 0.9996 | 0.9987 |
| | RMSE | 1.597 | 0.009233 |
| 3rd order | R-squared | 0.9999 | 0.9997 |
| | RMSE | 0.9871 | 0.004833 |
| 4th order | R-squared | 0.9999 | 0.9997 |
| | RMSE | 0.7626 | 0.004916 |
| 5th order | R-squared | 0.9999 | −7.102 |
| | RMSE | 0.7136 | 0.7967 |
| 6th order | R-squared | 0.9999 | −27630000 |
| | RMSE | 0.7572 | 1552 |

### 2.2. Electric motor part

Modeling for the electric motor was conducted in two steps. First, the motor performance was predicted, and then the load torque estimation based on the air compression performance was performed.

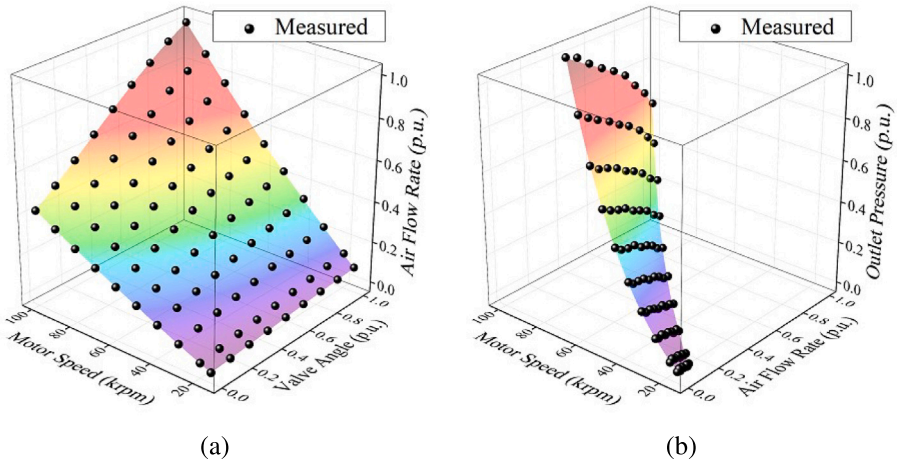


**Fig. 4.** Compression performance modeling result (a) air flow rate and (b) outlet pressure.

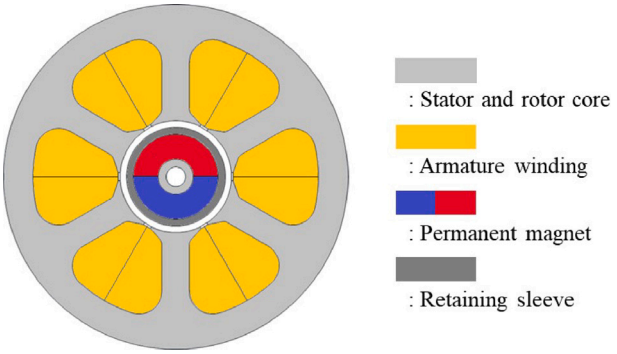


**Fig. 5.** Cross-sectional view of the electric motor for air compressor.

**Table 3**
Specifications of the air compressor motor.

| Items | Value | Unit | Note |
|---|---|---|---|
| Pole/Slot number | 2/6 | – | – |
| Maximum output power | 10 | kW | @100000 rpm |
| Maximum torque | 0.96 | Nm | – |
| Maximum speed | 100000 | rpm | – |
| Nominal DC voltage | 280 | V | – |
| Maximum current | 48.2 | $A_{rms}$ | – |
| Maximum current density | 8.5 | $A_{rms}/mm^2$ | – |

For the motor performance calculation, an electromagnetic finite element analysis (FEA)-based method was adopted. The type of target motor is a surface-mounted permanent magnet synchronous motor (SPMSM) with a retaining sleeve. Fig. 5 shows the cross-sectional area of this target UHS motor. Moreover, the specification of the target motor is organized in Table 3. The overall procedure is illustrated in Fig. 6. In addition, to calculate the output torque and efficiency considering the voltage limit, a $d-q$ axis equivalent circuit was adopted. Eqs. (1)–(4), which are given below, were used in the calculation [41].

$$\begin{bmatrix} v_d \\ v_q \end{bmatrix} = R_a \begin{bmatrix} i_{od} \\ i_{oq} \end{bmatrix} + \left(1 + \frac{R_a}{R_I}\right) \begin{bmatrix} v_{od} \\ v_{oq} \end{bmatrix} + p \begin{bmatrix} L_d & 0 \\ 0 & L_q \end{bmatrix} \begin{bmatrix} i_{od} \\ i_{oq} \end{bmatrix}$$
$$\begin{bmatrix} v_{od} \\ v_{oq} \end{bmatrix} = \begin{bmatrix} 0 & -\omega L_q \\ \omega L_d & 0 \end{bmatrix} \begin{bmatrix} i_d \\ i_q \end{bmatrix} + \begin{bmatrix} 0 \\ \omega \Psi_a \end{bmatrix} \quad (1)$$

$$T = P_p \left\{ \Psi_a i_{oq} + \left(L_d - L_q\right) i_{od} i_{oq} \right\} \quad (2)$$

$$W_C = R_a \left( i_d^2 + i_q^2 \right) \quad (3)$$

$$\eta_{em} = \frac{\omega_m T}{\omega_m T + W_C + W_I + W_E} \quad (4)$$

Here, $v_d$ and $v_q$ are the $d$ and $q$ axis voltages, respectively; $v_{od}$ and $v_{oq}$ are the induced voltages of the $d$ and $q$ axes, respectively; $i_d$ and $i_q$ are the armature currents of the $d$ and $q$ axes, respectively; $i_{od}$ and $i_{oq}$ are the iron loss-subtracted value of the $d$ and $q$ axis current, respectively; $R_a$ is the armature winding resistance; $R_I$ is the equivalent iron loss resistance; $L_d$ and $L_q$ are the $d$ and $q$ axis inductances, respectively; $\Psi_a$ is the linkage flux; $\omega$ is the electrical rotational angular speed; $p$ is the differential operator; $T$ is the torque; $P_p$ is the number of pole pairs; $W_C$, $W_I$, and $W_E$ are the copper loss, iron loss, and rotor eddy current loss, respectively; $\eta_{em}$ is the efficiency; and $\omega_m$ is the mechanical rotational angular speed.

From the two-Dimensional (2D) FEA, $L_d$, $L_q$, and $\Psi_a$ were calculated. In addition, based on the 2D FEA analysis results, the iron loss was calculated through a post-processing process [42]. Moreover, for the rotor eddy current loss calculation, a hybrid approach using a combination of the three-Dimensional (3D) FEA and analytical formulation was adopted [43].

In the case of load torque estimation, the previously calculated motor performance and experimentally measured data were utilized. First, according to the energy conservation law, the input power of the electric motor $W_{mot}$ can be calculated, as expressed in Eq. (5).

$$W_{mot} = \omega_m T + W_C + W_I + W_E \quad (5)$$

Next, the input power of the inverter $W_{inv}$ was determined from the measured power of the direct current (DC) power supply. Subsequently, the output power of the inverter could be calculated if the efficiency can be assumed. In this study, the efficiency of the inverter was assumed to be 98% constant, to make the assumption that the electric motor was in the worst condition [44–46]. Therefore, the input power of the motor $W_{mot}$ can be calculated according to Eq. (6), where $\eta_{inv}$ is the efficiency of the inverter. This procedure is shown in Fig. 7.

$$W_{mot} = W_{inv} \times \eta_{inv} \quad (6)$$

## 3. Thermal modeling

This section introduces the thermal modeling process based on the LPTN and optimization techniques. First, the concept of the LPTN and its application are presented. Subsequently, the screening methodology for the uncertain coefficients of the constructed LPTN is explained. Finally, the procedure for determining the uncertain coefficients is introduced using the surrogate model-based optimization approach.

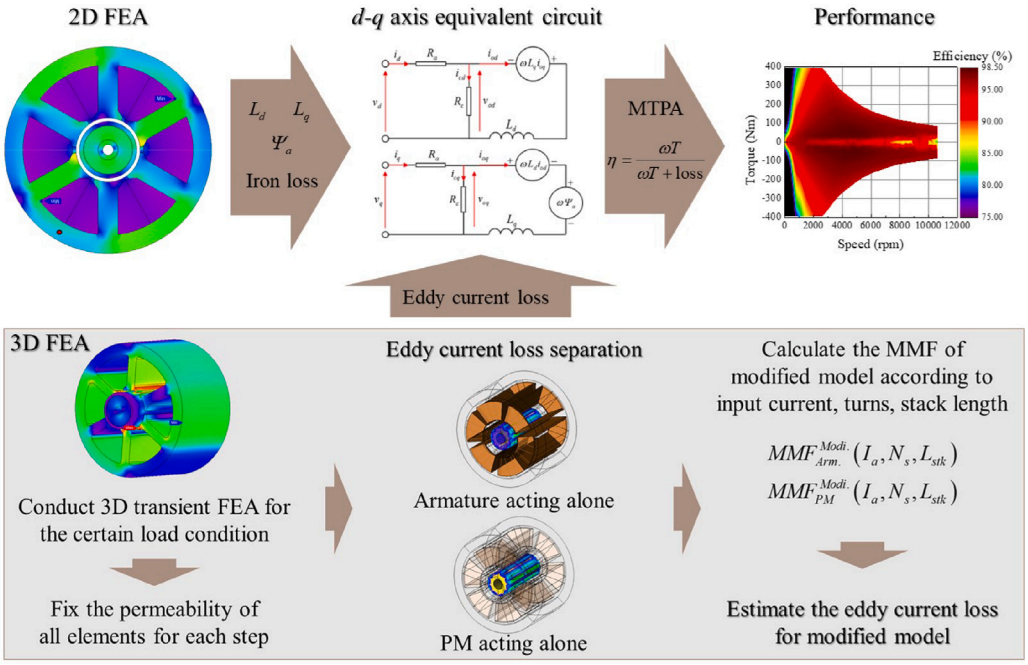


**Fig. 6.** Modeling process of electric motor performance.

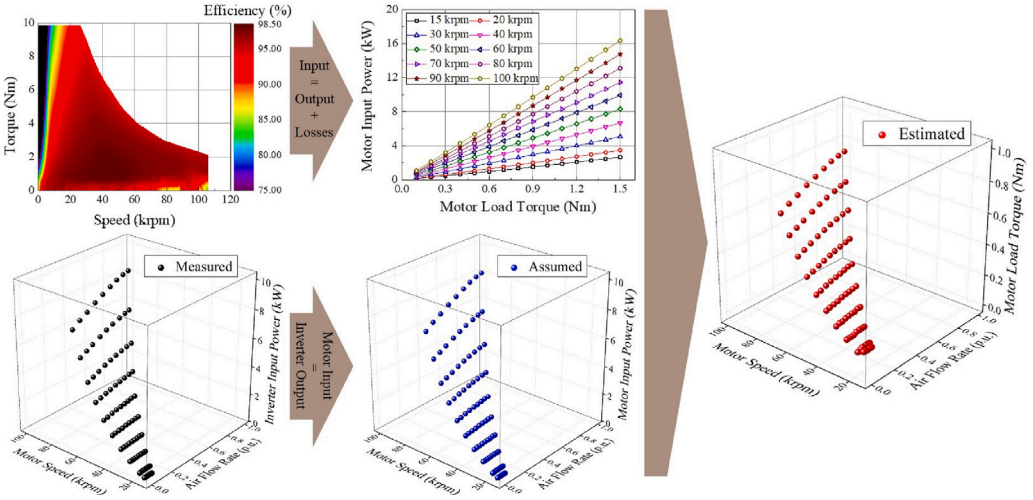


**Fig. 7.** Load torque modeling procedure for the electric motor.

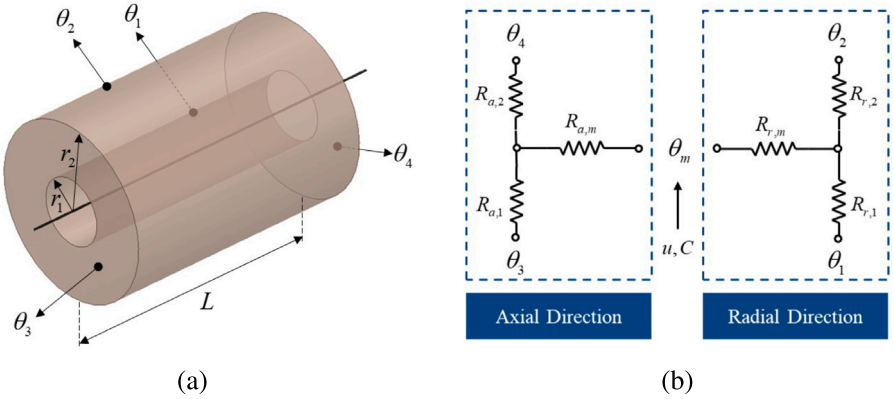


**Fig. 8.** Concept of lumped parameter thermal network (a) geometry assumption and (b) equivalent network.

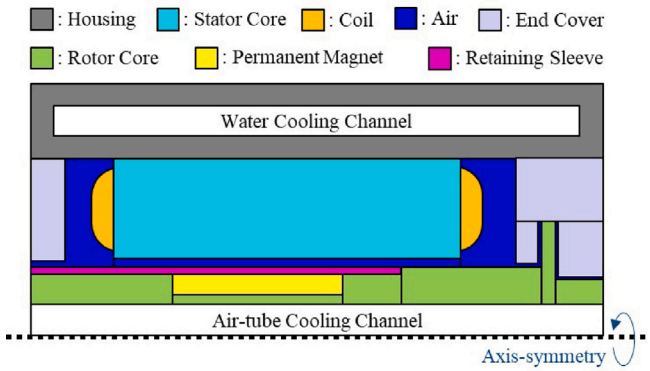


**Fig. 9.** Simplified structure of air supply system for lumped thermal modeling.

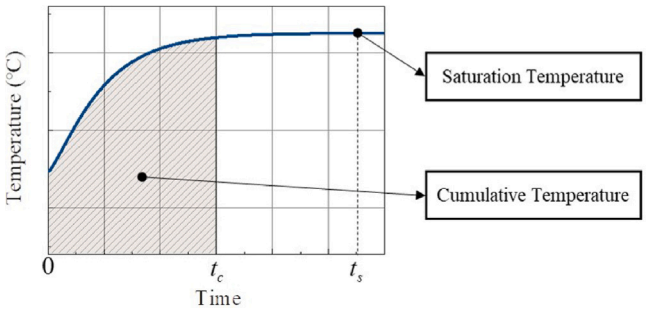


**Fig. 10.** Definition of the objective functions for uncertain coefficient screening.

### 3.1. Lumped parameter thermal network

The concept of the LPTN, adopted in this study was suggested by Mellor et al. [47]. As shown in Fig. 8(a), all components were modeled as cylindrical structures. The thermal flow was modeled in two directions, axial and radial, as shown in Fig. 8(b).

Here $\theta_1$ and $\theta_2$ are the inner and outer temperatures in the radial direction, respectively; $\theta_3$ and $\theta_4$ are the front and rear temperatures in the axial direction, respectively; $r_1$ and $r_2$ are the inner and outer radii of the lumped component, respectively; $L$ is the axial length of the lumped component; $\theta_m$ is the average temperature, which indicates the representative temperature of the lumped component; $R_{a,1}$ and $R_{a,2}$ are the thermal resistances for the axial direction heat flows; $R_{r,1}$ and $R_{r,2}$ are the thermal resistances for the radial direction heat flows; $R_{a,m}$ and $R_{r,m}$ are the compensation thermal resistances for the axial and radial direction heat flows; $u$ and $C$ represent the generated heat and the heat capacity of the lumped component, respectively.

Eqs. (7)–(12) express the thermal resistances and capacity. Here, $k_a$ and $k_r$ are the thermal conductivities in the axial and radial directions, respectively; $c$ is specific heat; and $\rho$ is the density.

$$R_{a,1} = R_{a,2} = \frac{L}{2\pi k_a \left(r_2^2 - r_1^2\right)} \tag{7}$$

$$R_{a,m} = -\frac{L}{6\pi k_a \left(r_2^2 - r_1^2\right)} \tag{8}$$

$$R_{r,1} = \frac{1}{4\pi k_r L}\left[1 - \frac{2r_1^2 \ln\left(\frac{r_2}{r_1}\right)}{\left(r_2^2 - r_1^2\right)}\right] \tag{9}$$

$$R_{r,2} = \frac{1}{4\pi k_r L}\left[\frac{2r_2^2 \ln\left(\frac{r_2}{r_1}\right)}{\left(r_2^2 - r_1^2\right)} - 1\right] \tag{10}$$

$$R_{r,m} = -\frac{1}{8\pi k_r \left(r_2^2 - r_1^2\right) L}\left[r_2^2 + r_1^2 - \frac{4r_1^2 r_2^2 \ln\left(\frac{r_2}{r_1}\right)}{\left(r_2^2 - r_1^2\right)}\right] \tag{11}$$

$$C = c\rho\pi L\left(r_2^2 - r_1^2\right) \tag{12}$$

To apply this cylindrical lumped thermal modeling strategy, the structure of the air supply system was simplified, as illustrated in Fig. 9. As shown in Fig. 9, water- and air-cooling channels were considered and modeled as heat dissipation components. In addition, the losses were reflected as the heat source components. Moreover, the contact planes were treated using the contact thermal resistance coefficients.

### 3.2. Uncertain coefficient screening

The LPTN was constructed with numerous resistances and coefficients. Most of these can be determined by the dimensions or material properties. However, several values cannot be determined easily. Table 4 lists the uncertain coefficients. This list includes air flow-related values, such as the air-bearing loss, thermal convection, air flow rate through the air-hole of the rotor shaft, and the air cooling channel formed in the armature winding coils. In addition, the contact thermal resistances, which depend on the manufacturing process, are included. In addition, their boundaries were determined and are also presented in Table 4.

The bearing loss-related coefficients were bounded based on the spindle test results. The maximum value of the inverter switch loss was calculated based on the equations of the conduction loss and switching loss [48]. Based on the study by Staton et al., natural convection heat coefficients were bounded and based on the study by Howey et al., Nerg et al., and Nachouane et al. [49–52]. In addition, the convective heat coefficients were bounded to describe the thin air layer and quasi-contact situation. Moreover, boundaries of contact thermal resistances were determined based on the study by Simpson et al., and Camilleri et al. [53,54]. The maximum value of the air-tube air flow rate was determined based on the CFD analysis results. And coil air cooling channel-related values came from physically possible ranges.

To conduct the uncertain coefficient determination described in Section 3.3, the screening process based on the $p$-value was performed. The $p$-value indicating the effectiveness of a particular response was derived from the analysis of variance (ANOVA) results [55].

To conduct the ANOVA, objective functions were first defined as shown in Fig. 10. To investigate both the transient and saturation characteristics, the cumulative temperature $T_c$ and saturation temperature $T_s$ were defined by Eqs. (13) and (14), respectively. Here, $t_c$ and $t_s$ are the minimum values satisfying Eqs. (15) and (16).

$$T_c = \int_0^{t_c} T(t)\,dt \tag{13}$$

$$T_s = T(t_s) \tag{14}$$

$$\frac{dT(t_c)}{dt} < 0.02 \tag{15}$$

$$\frac{dT(t_s)}{dt} < 0.001 \tag{16}$$

Next, the three-level near-orthogonal array (near-OA) table was adopted to conduct the design of experiment (DOE) for ANOVA. The used near-OA table is presented in Table 5. Here, 0 and 2 indicate the lower and upper boundary values, respectively, and 1 indicates the nominal value of the boundaries [56]. Next, the ANOVA was performed for the temperature responses from the LPTN. The p-values from this ANOVA are shown in Figs. 11 and 12.

**Table 4**
List of the uncertain coefficients for the lumped parameter thermal network.

| | Items | Boundary | |
|---|---|---|---|
| | | Lower | Upper |
| X0 | Thrust air-bearing total loss (W) | 600 | 700 |
| X1 | Front thrust air-bearing loss proportion (%) | 90 | 100 |
| X2 | Integrated inverter switch loss (W) | 0 | 912 |
| X3 | Housing radial direction convective heat transfer coefficient (W/m$^2$ °C) | 10 | 20 |
| X4 | Housing axial direction convective heat transfer coefficient (W/m$^2$ °C) | 10 | 20 |
| X5 | End cover air convective heat transfer coefficient (W/m$^2$ °C) | 20 | 300 |
| X6 | Housing-Stator contact thermal resistance coefficient (W/m$^2$ °C) | 200 | 6000 |
| X7 | Sleeve-Core(#1) contact thermal resistance coefficient (W/m$^2$ °C) | 200 | 6000 |
| X8 | Sleeve-PM contact thermal resistance coefficient (W/m$^2$ °C) | 200 | 6000 |
| X9 | Sleeve-Core(#2) contact thermal resistance coefficient (W/m$^2$ °C) | 200 | 6000 |
| X10 | Sleeve-Core(#3) contact thermal resistance coefficient (W/m$^2$ °C) | 200 | 6000 |
| X11 | Air-tube cooling channel air flow rate (LPM) | 0 | 150 |
| X12 | Coil air cooling channel area (mm$^2$) | 1.6 | 162.3 |
| X13 | Coil air cooling channel perimeter (m) | 0.01 | 1.03 |
| X14 | Core(#4)-End cover(#1) contact thermal resistance coefficient (W/m$^2$ °C) | 200 | 6000 |
| X15 | Front thrust air-bearing convective heat transfer coefficient (W/m$^2$ °C) | 10 | 1000 |
| X16 | Rear thrust air-bearing convective heat transfer coefficient (W/m$^2$ °C) | 10 | 1000 |
| X17 | Thrust air-bearing outer convective heat transfer coefficient (W/m$^2$ °C) | 10 | 1000 |
| X18 | Core(#5)-End cover(#2) contact thermal resistance coefficient (W/m$^2$ °C) | 200 | 6000 |

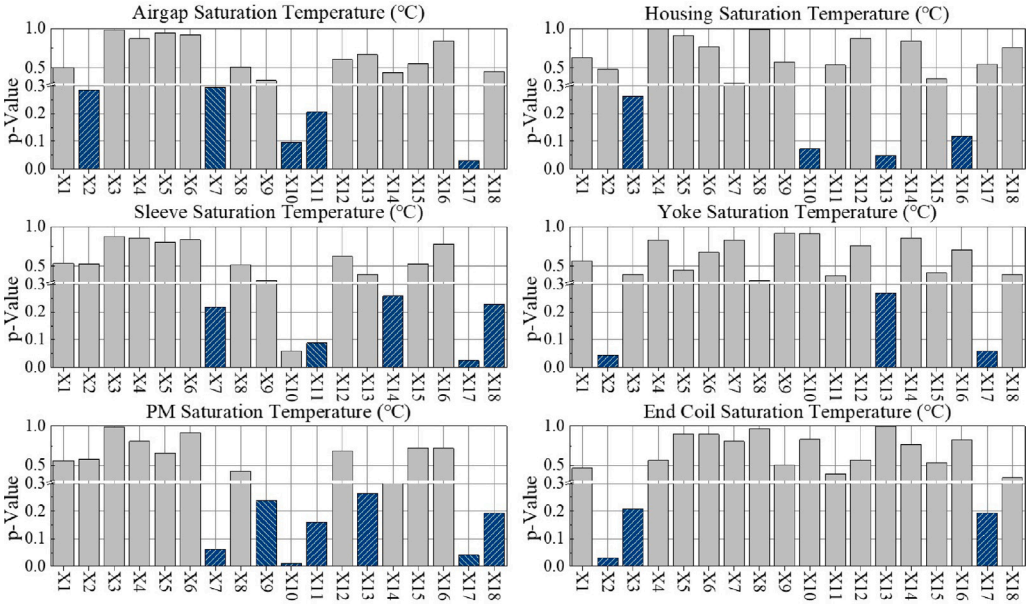


**Fig. 11.** p-values from the analysis of variance for the saturation temperatures.

The objective of this screening was to determine the coefficients that rarely affected the response. Therefore, the threshold for the *p*-value was set to 0.3 instead of 0.05, which is the value typically used to determine significance. Consequently, X5 and X9 were determined as the average values of the boundary [57].

### 3.3. Uncertain coefficient determination

This study determined the uncertain coefficient based on the surrogate model from the Gaussian process modeling (GPM). The temperature trace error between the experimentally measured result and estimated result from the LPTN was set as the objective function $f$. This is expressed in Eq. (17), where, $T_{EXP}$ and $T_{LPTN}$ are the temperatures obtained from the experiment and LPTN, respectively.

$$f = \int_0^{t_s} \left[T_{EXP}(t) - T_{LPTN}(t)\right]^2 dt \tag{17}$$

Next, to acquire the $T_{EXP}$, the temperature measurement test was preceded. The thermocouples were equipped as shown in Fig. 14. To reduce the electromagnetic field interference, the thermocouples with the twisted wire were used. To measure the temperature of the stator yokes, six thermocouples were attached at the center yoke of each phase at the front and rear. To fix the thermocouples tightly, we adopted adhesive which has a comparatively high thermal conductivity. In addition, to minimize the effect of adhesive on temperature, we attached thermocouples to the position which can cross the rear and front. And the recorded temperatures from the temperature measurement test are shown in Fig. 15. The average value of the recorded temperatures was designated as $T_{EXP}$, which indicates the reference temperature. Even though we adopted the thermocouple with twisted wire, there existed noise in some yoke positions, due to the stator yoke being in the magnetic flux path (see Fig. 13).

The temperature test was conducted using the same test bench used in the air compression test as shown in Fig. 4. The electric motor was continuously operated at a rotational speed of 100 krpm, and the inlet valve angle was set to achieve the maximum rated output power. Moreover, the temperature and flow rate of the water-cooling channel were maintained constantly using a water pump with a chiller.

In the next stage, the surrogate model of the objective function $f$ according to the screened uncertain coefficients was generated. The

**Table 5**
Three-level near orthogonal array table for uncertain coefficient screening.

| No. | X1 | X2 | X3 | X4 | X5 | X6 | X7 | X8 | X9 | X10 | X11 | X12 | X13 | X14 | X15 | X16 | X17 | X18 |
|---|---|---|---|---|---|---|---|---|---|---|---|---|---|---|---|---|---|---|
| 1 | 0 | 2 | 0 | 2 | 1 | 0 | 0 | 1 | 2 | 1 | 0 | 0 | 2 | 2 | 0 | 1 | 0 | 2 |
| 2 | 2 | 0 | 1 | 2 | 1 | 2 | 1 | 0 | 2 | 1 | 0 | 2 | 2 | 2 | 0 | 2 | 1 | 1 |
| 3 | 0 | 2 | 2 | 2 | 2 | 0 | 0 | 1 | 1 | 0 | 0 | 1 | 0 | 0 | 2 | 1 | 1 | 1 |
| 4 | 2 | 2 | 0 | 1 | 0 | 2 | 1 | 1 | 2 | 0 | 2 | 2 | 2 | 0 | 0 | 0 | 0 | 1 |
| 5 | 1 | 1 | 1 | 1 | 1 | 0 | 0 | 2 | 0 | 1 | 2 | 1 | 0 | 0 | 2 | 2 | 0 | 0 |
| 6 | 1 | 1 | 0 | 0 | 2 | 0 | 2 | 0 | 0 | 2 | 0 | 0 | 2 | 0 | 1 | 1 | 0 | 1 |
| 7 | 1 | 0 | 0 | 0 | 0 | 1 | 1 | 1 | 1 | 1 | 0 | 0 | 0 | 1 | 2 | 1 | 1 | 0 |
| 8 | 0 | 0 | 1 | 0 | 1 | 1 | 2 | 1 | 2 | 0 | 1 | 1 | 0 | 2 | 1 | 0 | 0 | 0 |
| 9 | 2 | 1 | 2 | 1 | 0 | 2 | 2 | 1 | 2 | 1 | 0 | 0 | 0 | 0 | 1 | 2 | 2 | 0 |
| 10 | 1 | 2 | 1 | 0 | 2 | 2 | 1 | 1 | 1 | 0 | 1 | 0 | 1 | 2 | 2 | 2 | 0 | 2 |
| 11 | 0 | 2 | 1 | 0 | 0 | 2 | 2 | 2 | 2 | 2 | 2 | 1 | 2 | 2 | 2 | 1 | 2 | 0 |
| 12 | 1 | 2 | 2 | 1 | 1 | 1 | 1 | 0 | 2 | 2 | 2 | 1 | 1 | 0 | 1 | 1 | 1 | 2 |
| 13 | 2 | 2 | 0 | 0 | 0 | 1 | 0 | 0 | 0 | 0 | 2 | 2 | 0 | 2 | 1 | 2 | 1 | 1 |
| 14 | 2 | 0 | 0 | 1 | 2 | 1 | 2 | 2 | 0 | 0 | 0 | 1 | 2 | 2 | 2 | 2 | 1 | 2 |
| 15 | 0 | 2 | 0 | 1 | 1 | 1 | 1 | 2 | 0 | 2 | 1 | 0 | 0 | 1 | 0 | 1 | 2 | 1 |
| 16 | 1 | 0 | 1 | 2 | 0 | 0 | 1 | 2 | 0 | 0 | 0 | 2 | 1 | 1 | 1 | 1 | 2 | 1 |
| 17 | 0 | 1 | 2 | 0 | 0 | 0 | 1 | 0 | 1 | 2 | 0 | 1 | 1 | 2 | 0 | 2 | 0 | 2 |
| 18 | 2 | 0 | 2 | 2 | 2 | 1 | 1 | 2 | 2 | 2 | 2 | 0 | 0 | 2 | 1 | 0 | 1 | 2 |
| 19 | 0 | 2 | 2 | 0 | 0 | 0 | 2 | 2 | 0 | 1 | 1 | 2 | 2 | 0 | 2 | 0 | 1 | 2 |
| 20 | 0 | 0 | 2 | 2 | 1 | 2 | 2 | 2 | 1 | 0 | 2 | 0 | 2 | 1 | 1 | 2 | 0 | 1 |
| 21 | 1 | 2 | 0 | 2 | 2 | 2 | 2 | 0 | 1 | 1 | 2 | 1 | 0 | 1 | 1 | 0 | 2 | 2 |
| 22 | 1 | 1 | 2 | 2 | 0 | 1 | 0 | 0 | 2 | 0 | 1 | 0 | 2 | 1 | 2 | 2 | 2 | 2 |
| 23 | 2 | 0 | 2 | 0 | 1 | 0 | 1 | 0 | 1 | 0 | 1 | 1 | 2 | 0 | 0 | 1 | 2 | 0 |
| 24 | 2 | 1 | 1 | 2 | 0 | 1 | 2 | 2 | 1 | 2 | 1 | 2 | 0 | 0 | 0 | 1 | 0 | 2 |
| 25 | 0 | 1 | 0 | 0 | 1 | 2 | 0 | 2 | 2 | 0 | 0 | 2 | 1 | 0 | 1 | 0 | 2 | 2 |
| 26 | 1 | 2 | 2 | 1 | 2 | 1 | 0 | 2 | 1 | 2 | 0 | 2 | 2 | 2 | 0 | 0 | 2 | 0 |
| 27 | 0 | 0 | 0 | 1 | 2 | 0 | 2 | 0 | 2 | 2 | 1 | 2 | 0 | 1 | 2 | 2 | 0 | 1 |
| 28 | 2 | 0 | 2 | 1 | 2 | 2 | 0 | 0 | 0 | 1 | 1 | 2 | 1 | 2 | 1 | 1 | 0 | 0 |
| 29 | 2 | 2 | 1 | 2 | 1 | 1 | 2 | 0 | 0 | 2 | 0 | 0 | 1 | 1 | 2 | 0 | 0 | 0 |
| 30 | 2 | 1 | 1 | 1 | 0 | 0 | 0 | 1 | 1 | 2 | 1 | 1 | 2 | 1 | 1 | 0 | 1 | 1 |
| 31 | 0 | 0 | 1 | 1 | 0 | 1 | 0 | 0 | 1 | 1 | 2 | 0 | 1 | 0 | 2 | 0 | 2 | 1 |
| 32 | 2 | 0 | 2 | 0 | 1 | 2 | 0 | 1 | 0 | 2 | 2 | 2 | 0 | 1 | 2 | 1 | 2 | 2 |
| 33 | 0 | 1 | 1 | 1 | 2 | 2 | 1 | 0 | 0 | 0 | 0 | 0 | 0 | 1 | 0 | 0 | 1 | 2 |
| 34 | 2 | 2 | 1 | 0 | 2 | 0 | 0 | 2 | 2 | 1 | 1 | 0 | 1 | 1 | 0 | 2 | 1 | 0 |
| 35 | 1 | 1 | 2 | 0 | 2 | 1 | 2 | 1 | 2 | 1 | 2 | 1 | 1 | 1 | 0 | 0 | 0 | 1 |
| 36 | 2 | 1 | 0 | 2 | 1 | 2 | 1 | 2 | 1 | 1 | 1 | 1 | 1 | 2 | 2 | 0 | 2 | 1 |
| 37 | 1 | 0 | 0 | 2 | 0 | 2 | 0 | 1 | 0 | 2 | 1 | 1 | 1 | 0 | 0 | 2 | 1 | 0 |
| 38 | 1 | 1 | 0 | 1 | 1 | 0 | 2 | 1 | 1 | 0 | 2 | 2 | 1 | 2 | 0 | 1 | 1 | 0 |
| 39 | 0 | 1 | 2 | 2 | 2 | 1 | 1 | 1 | 0 | 1 | 2 | 2 | 2 | 0 | 1 | 2 | 2 | 0 |

GPM was adopted for this process [58]. First, the DOE was conducted. Using the optimal Latin hypercube sampling, the initial sampling points were generated [59]. Next, considering the indicator of surrogate modeling quality, additional sampling was conducted [60]. In this study, the normalized RMSE (NRMSE) expressed in Eq. (18) was adopted for surrogate modeling quality criteria [61]. Here, $n_s$ is the number of sampling points, $\mathbf{x}$ and $\mathbf{Y}(\mathbf{x})$ are the vectors of the design variables and responses, respectively, $x_i$ and $Y(x_i)$ are the values of the design variables and responses at the $i$th sampling point, respectively, and $\hat{Y}^{(-i)}(x_i)$ is the forecast response of the $i$th sampling point from the GPM surrogate model, except for the $i$th sampling point. The DOE results are shown in Fig. 16.

$$\sqrt{\frac{1}{n_s}\sum_{i=1}^{n_s}\left(\frac{Y\left(x_i\right)-\hat{Y}^{(-i)}\left(x_i\right)}{\max\left\{\mathbf{Y}\left(\mathbf{x}\right)\right\}-\min\left\{\mathbf{Y}\left(\mathbf{x}\right)\right\}}\right)^2}\cdot 100\% \tag{18}$$

In addition, the formulation of the uncertain coefficient determination problem could be organized as follows.

Objective function : minimize $f(\mathbf{x})$

Design variables: $X0, X1, X2, X3, X4, X6, X7$

$X8, X10, X11, X12, X13, X14, X15, X16, X17, X18$

Subjected to

Variable bounds : $600 \le X0 \le 700,\ 90 \le X1 \le 100,$

$0 \le X2 \le 912,\ 10 \le X3, X4 \le 20,$

$200 \le X6, X7, X8, X10, X14, X18 \le 600,$

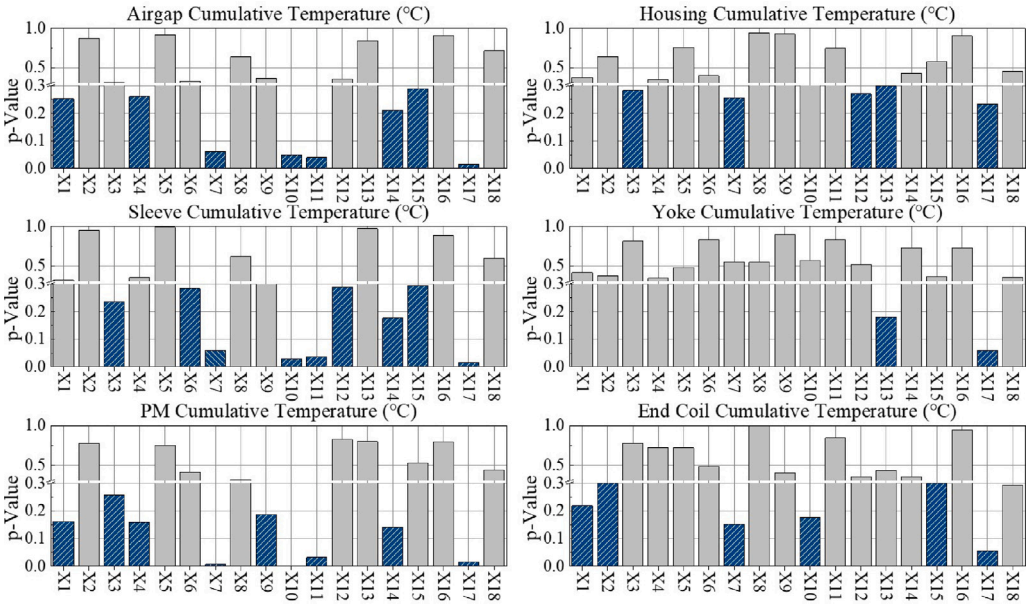


**Fig. 12.** p-values from the analysis of variance for the cumulative temperatures.

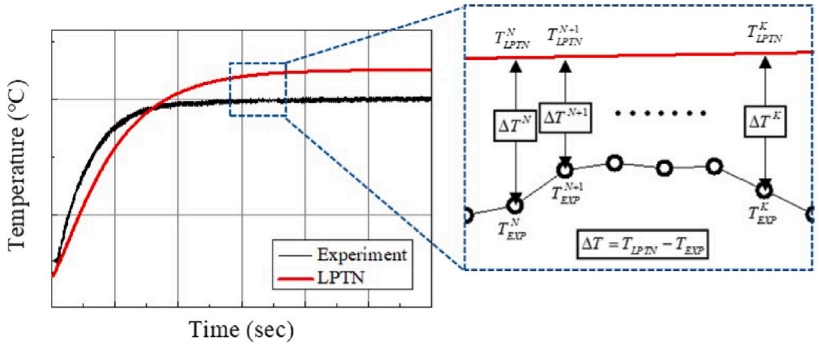


**Fig. 13.** Definition of the objective function for uncertain coefficient determination.

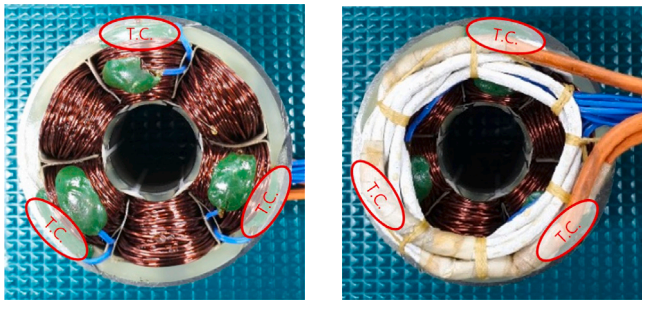


**Fig. 14.** Equipped thermocouples for temperature measurement on the (a) front and (b) rear.

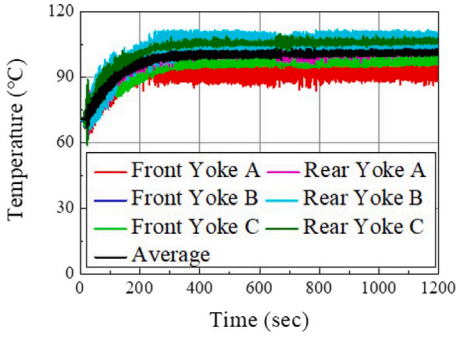


**Fig. 15.** Recorded temperatures from the front and rear thermocouples.

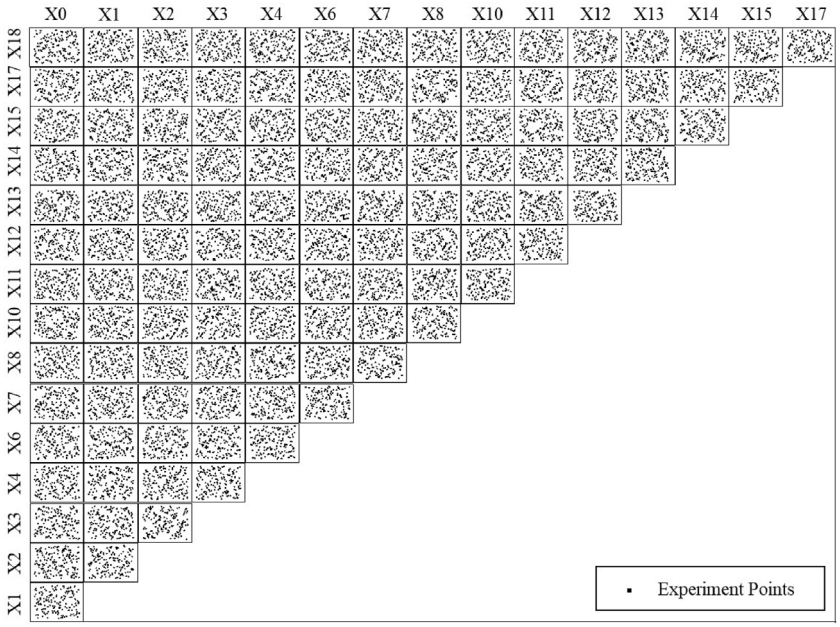


**Fig. 16.** Design of experiment result for objective function surrogate modeling based on optimal Latin hypercube sampling.

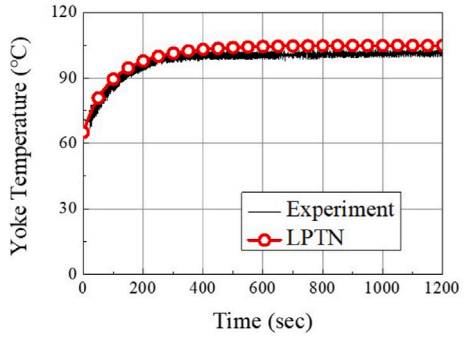


**Fig. 17.** Temperature estimation result from LPTN with determined uncertain coefficients.

$$0 \le X11 \le 150,\ 1.6 \le X12 \le 162.3,$$

$$0.01 \le X13 \le 1.03,\ 10 \le X15, X16, X17 \le 1000$$

## 4. Results

### 4.1. LPTN construction result

According to the formulated problem in Section 3.3, the uncertain coefficients of the LPTN were determined. Next, a temperature estimation was performed to reflect the determined uncertain coefficients. The results are shown in Fig. 17, compared with the measured temperature profile.

The difference between the saturation temperature from the experiment and the saturation temperature from the LPTN was 3.23 °C. This was the average value, and the difference fluctuated from 1.66 °C to 5.37 °C. This was due to the temperature data ripple from the recorder of the thermocouple. In addition, for the transient region, the minimum difference between the profiles from the experiment and LPTN profile was 0.0 °C, maximum difference was 7.15 °C, and average difference was 2.43 °C.

Moreover, in Table 6, the determined uncertain coefficients are listed. The plausibility of this determination can be confirmed by investigating several determined values.

Because air compressors are responsible for compressing air, the internal pressure is intrinsically higher than the external pressure. The target air compressor used in this study was a one-stage centrifugal compressor with a one-sided impeller. Therefore, the compression part receives an outward (frontward) force. Consequently, most of the friction loss of the thrust bearing was concentrated toward the front. Accordingly, the determined value of 95.9 for $X1$, which is the value of the front thrust air-bearing loss proportion, seems reasonable.

In addition, the well-contacted region conducts thermal energy well. Therefore, the contact thermal resistance coefficients of the well-contacted region were larger than those of the other regions. The sleeve of the rotor was assembled using shrink fitting with a larger amount of interference than that of the other parts. This resulted in a comparatively better contact with the sleeve than with the other parts. Hence, the fact that the determined values of $X7$, $X8$, and $X10$ were larger than those of the other contact thermal resistance coefficients seems appropriate.

### 4.2. Experimental verification

To confirm the reliability of the developed LPTN, additional temperature measurement was performed. The results of this additional test are shown in Fig. 18. Fig. 18(a) shows the temperature profile of the near-rotor air, and Fig. 18(b) shows the temperature profile of the end coil.

Note that the near-rotor air temperature is directly affected by the rotor temperature, which includes the permanent magnet temperature. The temperature of the permanent magnet affects the overall performance of the electric motor in an air supply system. Therefore, the near-rotor air temperature was selected as one of the experimental verification candidate. The thermocouple for this measurement was fixed to the housing inside of the air supply system, and the terminals of the thermocouple were placed as close as possible to the near-rotor air. The LPTN temperature of the air gap between the motor stator and the rotor were compared. The average difference between the saturation temperature from the experiment and LPTN was 4.14 °C, and the average difference between the transient area temperature from the experiment and LPTN was 7.88 °C.

**Table 6**
List of the uncertain coefficients and their determined values.

| | Items | Determined value |
|---|---|---|
| X0 | Thrust air-bearing total loss (W) | 684.5 |
| X1 | Front thrust air-bearing loss proportion (%) | 95.9 |
| X2 | IGBT loss (W) | 500.1 |
| X3 | Housing radial direction convective heat transfer coefficient ($W/m^2$ °C) | 19.1 |
| X4 | Housing axial direction convective heat transfer coefficient ($W/m^2$ °C) | 15.6 |
| X6 | Housing-Stator contact thermal resistance coefficient ($W/m^2$ °C) | 799.9 |
| X7 | Sleeve-Core(#1) contact thermal resistance coefficient ($W/m^2$ °C) | 3102.8 |
| X8 | Sleeve-PM contact thermal resistance coefficient ($W/m^2$ °C) | 2719.5 |
| X10 | Sleeve-Core(#3) contact thermal resistance coefficient ($W/m^2$ °C) | 4362.3 |
| X11 | Air-tube cooling channel air flow rate (LPM) | 65.2 |
| X12 | Coil air cooling channel area ($mm^2$) | 67.2 |
| X13 | Coil air cooling channel perimeter (m) | 0.92 |
| X14 | Core(#4)-End cover(#1) contact thermal resistance coefficient ($W/m^2$ °C) | 1811.8 |
| X15 | Front thrust air-bearing convective heat transfer coefficient ($W/m^2$ °C) | 624.6 |
| X16 | Rear thrust air-bearing convective heat transfer coefficient ($W/m^2$ °C) | 505 |
| X17 | Thrust air-bearing outer convective heat transfer coefficient ($W/m^2$ °C) | 230.7 |
| X18 | Core(#5)-End cover(#2) contact thermal resistance coefficient ($W/m^2$ °C) | 2261.8 |

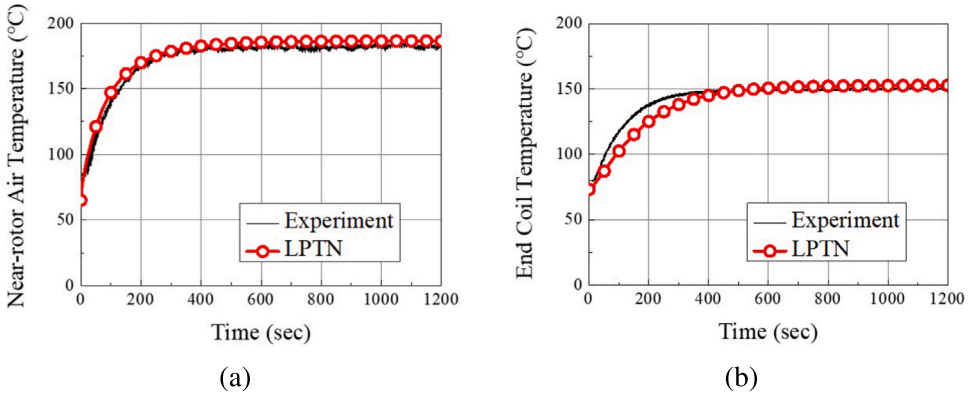


**Fig. 18.** Additional temperature measurement result (a) near-rotor air temperature profile (b) end coil temperature profile.

The other candidate for the experimental verification was the temperature of the end coil. To prevent burnout of the coils, the end coil temperature is typically monitored as the derating criteria. A total of six thermocouples were attached as the green adhesive substances at the smaller radius position of the thermocouple for measuring the yoke temperature, as shown in Fig. 14 of Section 3. The average values of the recorded temperature and LPTN temperature of the end coil were compared. The average difference between the saturation temperature from the experiment and LPTN was 2.10 °C, and the average difference between the transient area temperature from the experiment and LPTN was 10.19 °C.

The larger temperature error for the transient area came from the lumped parameterization. Especially, the more the modeling target complex, the more the temperature error of the transient period would occur. The lumped parameter could not describe the partial concentration of thermal energy. Therefore, if there is a large amount of thermal energy concentration in the modeling target, the temperature difference could occur during the transient region. This can be resolved by modeling the lumped parameter finer. Finer modeling could consider thermal concentration in more detail. However, the complex LPTN has no merit because of the larger computing time.

## 5. Conclusion

This study proposed a temperature estimation process for the air supply system of the PEM FC stack in FCEVs. First, the performance modeling of the air supply system was conducted. An empirical approach was adopted for the compression performance modeling. Electromagnetic FEA was used to model the performance of the electric motor of the air compressor driver. Subsequently, thermal modeling of the air supply system was performed. To apply the LPTN concept, the geometry of the air supply system was simplified. Subsequently, the LPTN of the air supply system was built. The uncertain coefficients such as the air flow rate through the rotor air-hole, contact thermal resistance coefficients, and coefficients related to convective thermal transfer were listed. Next, using the p-values from the ANOVA, the uncertain coefficient screening was conducted. Finally, without the excepted uncertain coefficients, a surrogate model-based coefficient determination was conducted. Finally, the LPTN construction result was investigated. Moreover, an additional experiment was conducted, and the validity of this suggestion was confirmed. According to the result, we can conclude that the suggested process can construct the LPTN from little amount of temperature data.

As the method proposed in this study is based on an analytical approach, the computing cost of this temperature estimation is very low. Therefore, the results of this study can be applied not only in the design process of the air supply system but also in the thermal or energy management of the air supply system. In addition, this study could be expanded to the overall fuel cell electric vehicle. If then, a new study could be achieved, that deals with the overall thermal and energy management of the vehicle system.

## CRediT authorship contribution statement

**Dong-Min Kim:** Conceptualization, Methodology, Formal analysis, Writing – original draft. **Jun-Woo Chin:** Methodology, Software. **Jae-Hyun Kim:** Formal analysis, Investigation, Writing – review & editing. **Myung-Seop Lim:** Writing – review & editing, Supervision.

## Declaration of competing interest

The authors declare that they have no known competing financial interests or personal relationships that could have appeared to influence the work reported in this paper.

## Data availability

No data was used for the research described in the article.

## Acknowledgment

This results was supported by "Regional Innovation Strategy (RIS)" through the National Research Foundation of Korea (NRF) funded by the Ministry of Education (MOE) (2021RIS-002).

## References

[1] United Nations Climate Change. The Paris Agreement and NDCs. 2023, https://unfccc.int/process-and-meetings/the-paris-agreement/nationally-determined-contributions-ndcs/nationally-determined-contributions-ndcs. [Accesed 26 July 2023].

[2] Volvo Cars Global Newsroom. Volvo cars to be fully electric by 2030. 2023, https://www.media.volvocars.com/global/en-gb/media/pressreleases/277409/volvo-cars-to-be-fully-electric-by-2030. [Accesed 26 July 2023].

[3] Li K, Wang L. Optimal electric vehicle subsidy and pricing decisions with consideration of EV anxiety and EV preference in green and non-green consumers. Transp Res E 2023;170:103010. http://dx.doi.org/10.1016/j.tre.2022.103010.

[4] TOYOTA Global Newsroom. Toyota developing hydrogen engine technologies through motorsports. 2023, https://global.toyota/en/newsroom/corporate/35209996.html?_ga=2.258506058.1359459145.1675091107-217118307.1675091107. [Accesed 26 July 2023].

[5] Toktaş-Palut P. The fuel cell electric vehicle market growth: Analyses of contracts and government incentives. Comput Ind Eng 2023;176:108988. http://dx.doi.org/10.1016/j.cie.2023.108988.

[6] Lee D-Y, Elgowainy A, Kotz A, Vijayagopal R, Marcinkoski J. Life-cycle implications of hydrogen fuel cell electric vehicle technology for medium- and heavy-duty trucks. J Power Sources 2018;393:217–29. http://dx.doi.org/10.1016/j.jpowsour.2018.05.012.

[7] Harvey LD. Resource implications of alternative strategies for achieving zero greenhouse gas emissions from light-duty vehicles by 2060. Appl Energy 2018;212:663–79. http://dx.doi.org/10.1016/j.apenergy.2017.11.074.

[8] Chen H, Liu Z, Ye X, Yi L, Xu S, Zhang T. Air flow and pressure optimization for air supply in proton exchange membrane fuel cell system. Energy 2022;238:121949. http://dx.doi.org/10.1016/j.energy.2021.121949.

[9] Hoeflinger J, Hofmann P. Air mass flow and pressure optimisation of a PEM fuel cell range extender system. Int J Hydrogen Energy 2020;45(53):29246–58. http://dx.doi.org/10.1016/j.ijhydene.2020.07.176.

[10] Qin Y, Du Q, Fan M, Chang Y, Yin Y. Study on the operating pressure effect on the performance of a proton exchange membrane fuel cell power system. Energy Convers Manage 2017;142:357–65. http://dx.doi.org/10.1016/j.enconman.2017.03.035.

[11] Han J, Yu S, Yi S. Adaptive control for robust air flow management in an automotive fuel cell system. Appl Energy 2017;190:73–83. http://dx.doi.org/10.1016/j.apenergy.2016.12.115.

[12] Xu J, Zhang C, Fan R, Bao H, Wang Y, Huang S, et al. Modelling and control of vehicle integrated thermal management system of PEM fuel cell vehicle. Energy 2020;199:117495. http://dx.doi.org/10.1016/j.energy.2020.117495.

[13] Wang J, Han Y, Pan S, Wang Z, Cui D, Geng M. Design and development of an oil-free double-scroll air compressor used in a PEM fuel cell system. Renew Energy 2022;199:840–51. http://dx.doi.org/10.1016/j.renene.2022.08.154.

[14] Wang C, Liu M, Wang B, Xing Z, Shu Y. Research on power consumption distribution characteristics of a water-lubricated twin-screw air compressor for fuel cell applications. Energy 2022;256:124673. http://dx.doi.org/10.1016/j.energy.2022.124673.

[15] Geng M, Wang L, Cui D, Li X, Li J, Jiang H. Profile design of twin screw air compressor for fuel cell. Energy Rep 2022;8:21–6. http://dx.doi.org/10.1016/j.egyr.2022.03.047.

[16] He Y, Xing L, Zhang Y, Zhang J, Cao F, Xing Z. Development and experimental investigation of an oil-free twin-screw air compressor for fuel cell systems. Appl Therm Eng 2018;145:755–62. http://dx.doi.org/10.1016/j.applthermaleng.2018.09.064.

[17] Liu Y, Zhao Y, Yang Q, Liu G, Li L, Gao Z. Performance study of centrifugal air compressor for proton exchange membrane fuel cell systems. Energy Sci Eng 2022;10(1):208–18. http://dx.doi.org/10.1002/ese3.1023.

[18] Zhang Y, Xu S, Wan Y. Performance improvement of centrifugal compressors for fuel cell vehicles using the aerodynamic optimization and data mining methods. Int J Hydrogen Energy 2020;45(19):11276–86. http://dx.doi.org/10.1016/j.ijhydene.2020.02.026.

[19] Shi T, Huang H, Peng X, Feng J, Guo Y. Experimental study on the static and dynamic performances of gas foil bearings for the centrifugal air compressor used in fuel cell vehicles. Int J Energy Res 2022;46(4):4417–33. http://dx.doi.org/10.1002/er.7439.

[20] Hu D, Yang L, Yi F, Hu L, Yang Q, Zhou J. Optimization of speed response of super-high-speed electric air compressor for hydrogen fuel cell vehicle considering the transient current. Int J Hydrogen Energy 2021;46(53):27183–92. http://dx.doi.org/10.1016/j.ijhydene.2021.05.169.

[21] Kim J-H, Kim D-M, Jung Y-H, Lim M-S. Design of ultra-high-speed motor for FCEV air compressor considering mechanical properties of rotor materials. IEEE Trans Energy Convers 2021;36(4):2850–60. http://dx.doi.org/10.1109/TEC.2021.3062646.

[22] Zhu Z, Deng J, Ouyang H, Dou X. Optimized sampling mechanism for full-state feedback current control of LCL-equipped high-speed PMSMs for fuel cell air compressor. IEEE Trans Transp Electr 1. http://dx.doi.org/10.1109/TTE.2022.3218153, Early Access.

[23] Kim S, Jeong H, Lee H. Cold-start performance investigation of fuel cell electric vehicles with heat pump-assisted thermal management systems. Energy 2021;232:121001. http://dx.doi.org/10.1016/j.energy.2021.121001.

[24] Hu D, Liu J, Yi F, Yang Q, Zhou J. Enhancing heat dissipation to improve efficiency of two-stage electric air compressor for fuel cell vehicle. Energy Convers Manage 2022;251:115007. http://dx.doi.org/10.1016/j.enconman.2021.115007.

[25] Im S-Y, Park S-H, Kim J-H, Chin J-W, Cha K-S, Lim M-S. Temperature prediction of ultra-high-speed SPMSM for FCEV air compressor considering PWM current harmonics. In: 2021 IEEE vehicle power and propulsion conference. 2021, p. 1–6. http://dx.doi.org/10.1109/VPPC53923.2021.9699318.

[26] Li L, Liu S, Shang Y, Xue M, Liu T, Zhu G. End-winding wire-insulation heat conduction model for precise thermal predictions of permanent magnet synchronous machines. IET Electr Power Appl 2023. http://dx.doi.org/10.1049/elp2.12339, Early View.

[27] Le W, Lin M, Lin K, Jia L, Yang A. Design and analysis of a rotor air-cooling enhanced method for axial flux permanent magnet machine with housing-cooling. IEEE Trans Energy Convers 2023;Early Access:1–10. http://dx.doi.org/10.1109/TEC.2023.3265676.

[28] Cao L, Fan X, Li D, Kong W, Qu R, Liu Z. Improved LPTN-based online temperature prediction of permanent magnet machines by global parameter identification. IEEE Trans Ind Electron 2023;70(9):8830–41. http://dx.doi.org/10.1109/TIE.2022.3208600.

[29] Gronwald P-O, Wiese N, Kern TA, Henke M. Electric traction motor spray cooling—Empirical model development and experimental validation. IEEE Trans Transp Electr 2023;9(2):2185–94. http://dx.doi.org/10.1109/TTE.2022.3206031.

[30] Park MH, Kim SC. Development and validation of lumped parameter thermal network model on rotational oil spray cooled motor for electric vehicles. Appl Therm Eng 2023;225:120176. http://dx.doi.org/10.1016/j.applthermaleng.2023.120176.

[31] Sun L, Gan H, Xiao X. Static sensor assisted rotor temperature estimation of permanent magnet machine for the low-speed servo applications. IET Electr Power Appl 2023;17(5):593–606. http://dx.doi.org/10.1049/elp2.12296.

[32] Liu W, Yang H, Lin H, Peng F, Lyu S, Huang X. Thermal modeling and analysis of hybrid-magnetic-circuit variable flux memory machine. IEEE Trans Ind Appl 2023;59(2):1307–18. http://dx.doi.org/10.1109/TIA.2022.3192357.

[33] Wöckinger D, Bramerdorfer G, Drexler S, Vaschetto S, Cavagnino A, Tenconi A, et al. Measurement-based identification of lumped parameter thermal networks for sub-Kw outer rotor PM machines. IEEE Trans Ind Appl 2023;59(1):823–33. http://dx.doi.org/10.1109/TIA.2022.3217029.

[34] Chen Q, Fan Y, Chen J, Lei Y, Yang C. A new analytical thermal model of distributed winding wheel machine for electric vehicles. IEEE Trans Veh Technol 2022;71(12):12691–700. http://dx.doi.org/10.1109/TVT.2022.3197903.

[35] Wang R, Fan X, Li D, Qu R, Li L, Zou T. Convective heat transfer characteristics on end-winding of stator immersed oil-cooled electrical machines for aerospace applications. IEEE Trans Transp Electr 2022;8(4):4265–78. http://dx.doi.org/10.1109/TTE.2022.3186800.

[36] Zhang Y, Ma T, Yang Y, Liang Y. Rotor temperature monitoring and torque correction for IPMSM of new energy vehicle. In: SAE 2022 vehicle electrification and powertrain diversification technology forum. 2022, http://dx.doi.org/10.4271/2022-01-7063.

[37] Jeffrey AJ, Connor PH, Vakil G, Evans P, Wheeler P, Hart S. Cooling system sizing using LPTN analysis and multiphysics modelling for an axial flux machine and integrated drive. In: 2022 international conference on electrical machines. 2022, p. 1376–82. http://dx.doi.org/10.1109/ICEM51905.2022.9910820.

[38] Chattopadhyay R, Islam MS, Jung J, Mikail R, Husain I. Winding embedded liquid cooling for slotless motors in transportation applications. IEEE Trans Ind Appl 2022;58(6):7110–20. http://dx.doi.org/10.1109/TIA.2022.3191629.

[39] Sequeira S, Bennion K, Cousineau JE, Narumanchi S, Moreno G, Kumar S, et al. Validation and parametric investigations of an internal permanent magnet motor using a lumped parameter thermal model. J Electron Packag 2022;144(2):021114. http://dx.doi.org/10.1115/1.4053121.

[40] Zarghani A, Torkaman H, Arbab N, Sedigh Toulabi M. Lumped parameter thermal network for thermal analysis of a rotor-excited axial flux switching machine with electromagnetic-thermal design. Measurement 2022;193:110971. http://dx.doi.org/10.1016/j.measurement.2022.110971.

[41] Kim D-M, Lee S-G, Kim D-K, Park M-R, Lim M-S. Sizing and optimization process of hybrid electric propulsion system for heavy-duty vehicle based on Gaussian process modeling considering traction motor characteristics. Renew Sustain Energy Rev 2022;161:112286. http://dx.doi.org/10.1016/j.rser.2022.112286.

[42] Kim D-M, Chin J-W, Hong J-P, Lim M-S. Performance prediction of surface-mounted permanent magnet synchronous motor based on ring specimen test result. IET Electr Power Appl 2019;13(9):1280–6. http://dx.doi.org/10.1049/iet-epa.2018.5382.

[43] Kim D-M, Kim J-H, Lee S-G, Park M-R, Lee G-H, Lim M-S. Estimation method for rotor eddy current loss in ultrahigh-speed surface-mounted permanent magnet synchronous motor. IEEE Trans Magn 2021;57(2):1–5. http://dx.doi.org/10.1109/TMAG.2020.3030684.

[44] Perdikakis W, Scott MJ, Yost KJ, Kitzmiller C, Hall B, Sheets KA. Comparison of si and SiC EMI and efficiency in a two-level aerospace motor drive application. IEEE Trans Transp Electr 2020;6(4):1401–11. http://dx.doi.org/10.1109/TTE.2020.3010499.

[45] Fu Y, Takemoto M, Ogasawara S, Orikawa K. Investigation of operational characteristics and efficiency enhancement of an ultrahigh-speed bearingless motor at 100 000 r/min. IEEE Trans Ind Appl 2020;56(4):3571–83. http://dx.doi.org/10.1109/TIA.2020.2986453.

[46] Pulsinelli F, di Benedetto M, Lidozzi A, Solero L, Crescimbini F. Power losses distribution in SiC inverter based electric motor drives. IEEE Trans Ind Appl 2019;55(6):7843–53. http://dx.doi.org/10.1109/TIA.2019.2941864.

[47] P.H. Mellor DT. Lumped parameter thermal model for electrical machines of TEFC design. IEE Proc B 1991;138. http://dx.doi.org/10.1049/ip-b.1991.0025, 205–218(13).

[48] Kwon K, Lee J-H, Lim S-K. Optimization of multi-speed transmission for electric vehicles based on electrical and mechanical efficiency analysis. Appl Energy 2023;342:121203. http://dx.doi.org/10.1016/j.apenergy.2023.121203.

[49] Staton DA, Cavagnino A. Convection heat transfer and flow calculations suitable for electric machines thermal models. IEEE Trans Ind Electron 2008;55(10):3509–16. http://dx.doi.org/10.1109/TIE.2008.922604.

[50] Howey DA, Childs PRN, Holmes AS. Air-gap convection in rotating electrical machines. IEEE Trans Ind Electron 2012;59(3):1367–75. http://dx.doi.org/10.1109/TIE.2010.2100337.

[51] Nerg J, Rilla M, Pyrhonen J. Thermal analysis of radial-flux electrical machines with a high power density. IEEE Trans Ind Electron 2008;55(10):3543–54. http://dx.doi.org/10.1109/TIE.2008.927403.

[52] Nachouane AB, Abdelli A, Friedrich G, Vivier S. Numerical study of convective heat transfer in the end regions of a totally enclosed permanent magnet synchronous machine. IEEE Trans Ind Appl 2017;53(4):3538–47. http://dx.doi.org/10.1109/TIA.2017.2691731.

[53] Simpson N, Duggan T, Mellor PH, Booker JD. Measurement of the thermal characteristics of a stator-housing interface. In: 2017 IEEE 11th international symposium on diagnostics for electrical machines, power electronics and drives. 2017, p. 557–64. http://dx.doi.org/10.1109/DEMPED.2017.8062410.

[54] Camilleri R, Howey D, McCulloch M. Experimental investigation of the thermal contact resistance in shrink fit assemblies with relevance to electrical machines. In: 7th IET international conference on power electronics, machines and drives. 2014, p. 1–9. http://dx.doi.org/10.1049/cp.2014.0472.

[55] Ståhle L, Wold S. Analysis of variance (ANOVA). Chemometr Intell Lab Syst 1989;6(4):259–72. http://dx.doi.org/10.1016/0169-7439(89)80095-4.

[56] Jones B, Lekivetz R, Majumdar D, Nachtsheim CJ, Stallrich JW. Construction, properties, and analysis of group-orthogonal supersaturated designs. Technometrics 2020;62(3):403–14. http://dx.doi.org/10.1080/00401706.2019.1654926.

[57] Wasserstein RL, Lazar NA. The ASA statement on p-values: Context, process, and purpose. Amer Statist 2016;70(2):129–33. http://dx.doi.org/10.1080/00031305.2016.1154108.

[58] Jones B, Johnson RT. Design and analysis for the Gaussian process model. Qual Reliab Eng Int 2009;25(5):515–24. http://dx.doi.org/10.1002/qre.1044.

[59] Sacks J, Welch WJ, Mitchell TJ, Wynn HP. Design and analysis of computer experiments. Stat Sci 1989;4(4):409–23.

[60] Kim S, Lee S-G, Kim J-M, Lee TH, Lim M-S. Robust design optimization of surface-mounted permanent magnet synchronous motor using uncertainty characterization by bootstrap method. IEEE Trans Energy Convers 2020;35(4):2056–65.

[61] Queipo NV, Haftka RT, Shyy W, Goel T, Vaidyanathan R, Tucker PK. Surrogate-based analysis and optimization. Prog Aerosp Sci 2005;41(1):1–28.